ACS Energy LETTERS

http://pubs.acs.org/journal/aelccp

Triphasic Electrolytes for Membrane-Free High-Voltage Redox Flow Battery

Rajeev K. Gautam, Xiao Wang, Soumalya Sinha, and Jianbing Jimmy Jiang*

Cite This: *ACS Energy Lett.* 2024, 9, 218−225

Read Online

ACCESS | Metrics & More | Article Recommendations | Supporting Information

ABSTRACT: **Liquid/liquid biphasic batteries without a membrane could be promising models of redox flow batteries. However, such batteries inherently undergo self-discharge at the liquid/liquid interface, resulting in a low Coulombic efficiency and poor capacity retention. Herein, we report a triphasic system comprising all-nonaqueous electrolytes to overcome the challenges in biphasic systems. By incorporation of a third electrolyte layer to separate the anolyte and catholyte, the system effectively impeded the self-discharge event without compromising the Coulombic efficiency and capacity retention. Li metal anode and phenothiazine derivative C18-PTZ (0.5 M) cathode have been used to construct the electrochemical cell. Moreover, we have designed two all-nonaqueous triphasic models either stacking the phases vertically or physically separating two phases sidewise along with a common interfacial layer at the top. Interestingly, both designs showed high capacity retention under static (∼98%, 31 days, 100 cycles) and flow (∼99%, 39 days, 100 cycles) conditions. Moreover, all batteries exhibited an average Coulombic efficiency of nearly 100%.**

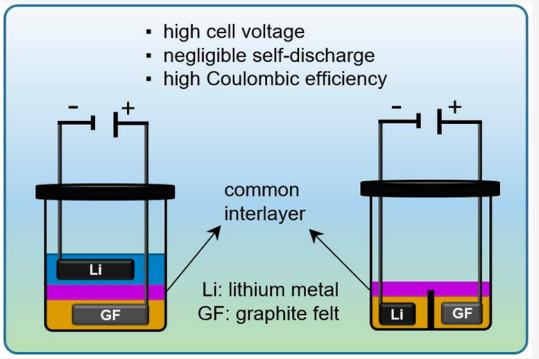

Global energy and climate challenges require the transition from fossil fuels to renewable energy resources, including but not limited to solar, wind, and hydroelectric power, driving the utilization of large-scale energy storage devices.[1−3] Redox flow batteries (RFBs) could be promising energy storage devices due to their unique properties, including high scalability, decoupled energy and power, and high safety.[4−6] In the conventional RFB configuration, redox-active materials are dissolved in solvents to form a catholyte and anolyte, which are stored separately in external tanks.[7] Depending on the electrolyte used, RFBs can be classified as either aqueous RFBs (ARFBs) or nonaqueous RFBs (NRFBs).[8−10] Although ARFBs are safer and more cost-effective, they typically have a narrow voltage window (<1.6 V) due to the low thermodynamic stability of water.[11,12] In contrast, NRFBs have a higher electrochemical window (∼5.5 V), but they are associated with other challenges such as low ionic conductivity, high flammability, and the high cost of organic electrolytes.[13,14] Additionally, NRFBs face the significant challenge of redoxmer crossover due to the lack of appropriate membranes in nonaqueous media, ultimately impacting the overall battery performance.[15−17] To optimize RFB performance, it is crucial to develop membranes with high ionic conductivity, molecular selectivity, stability, and low cost.[18,19]

An alternative strategy to address the aforementioned issues is the fabrication of RFBs without a membrane separator.[20,21] This approach, demonstrated by our group[22,23] and several other researchers,[24−29] involves utilizing immiscible aqueous/nonaqueous electrolytes. This biphasic system consists of two immiscible electrolytes with different densities and a suitable partition coefficient, forming two phases with a common interface. This interface functions as a separator between the anolyte and the catholyte.[20] However, membrane-free batteries with nonaqueous/nonaqueous electrolytes are rarely reported because of challenges in designing and selecting suitable solvents and redox-active materials.[30−32] Although membrane-free biphasic batteries are promising, they face significant challenges that limit their practical application. These challenges include capacity loss due to the mixing of the anolyte and catholyte at the interface, self-discharge induced by interfacial ion migration during the solvation−desolvation process (rate of solvent diffusion), and low capacity utilization owing to poor mass transfer under static conditions. Additionally, compared with membrane-based RFBs, membrane-free batteries exhibit an unstable liquid/liquid interface that can significantly disrupt the thermodynamic balance under

Received: November 30, 2023
Revised: December 8, 2023
Accepted: December 14, 2023

https://doi.org/10.1021/acsenergylett.3c02594
ACS Energy Lett. 2024, 9, 218−225

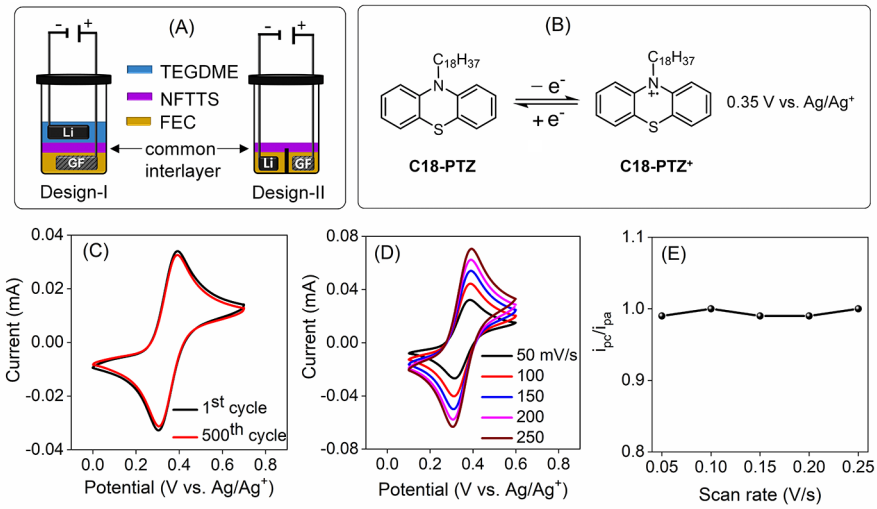

Figure 1. (A) Schematic of the triphasic systems (Design-I and -II). (B) Redox reactions of C18-PTZ. (C) Cyclic voltammograms were measured by repeated potential sweeping of 5 mM C18-PTZ in FEC/LiTFSI (0.1 M) on a glassy carbon electrode at a scan rate of 50 mV/s. (D) Cycling voltammetry stability of C18-PTZ in a FEC/LiTFSI (0.1 M) solution at different scan rates in the range of 50−250 mV/s. (E) The ratio of the reduction and oxidation peak currents is a function of scan rate.

flow conditions.[33,34] Active material crossover by convective mass transport under flow conditions further exacerbates capacity loss.

This study presents a new strategy by introducing a third layer as an ion-selective membrane to facilitate the separation of the anolyte and catholyte, alleviate self-discharge, and achieve a high Coulombic efficiency. The introduction of an interfacial electrolyte layer in the liquid/liquid triphasic system not only effectively separates the anolyte and catholyte but also facilitates convenient electrolyte flow (anolyte or catholyte) without disturbing the thermodynamic balance of the electrolyte phases even at high flow rates. This new approach enables the triphasic system to overcome the limitations of biphasic membrane-free batteries, resulting in improved capacity utilization and performance under flow conditions. The triphasic all-nonaqueous strategy is implemented using two distinct cell designs (see Figure 1A). Three nonaqueous electrolytes, tetraethylene glycol dimethyl ether (TEGDME), nonafluoro-1,1,2,2-tetrahydrohexyl-trimethoxysilane (NFTTS), and fluoroethylene carbonate (FEC), are used in the membrane-free batteries with Li metal and a phenothiazine derivative as the anode and cathode materials, respectively, resulting in a cell voltage of 3.52 V. The cycling performances of triphasic membrane-free batteries based on both designs are evaluated under static and flow conditions. All batteries exhibited outstanding cycling performances with capacity retentions under static conditions (~98%, 31 days, 100 cycles) and flow conditions (~99%, 39 days, 100 cycles). Furthermore, all of the batteries demonstrated an average Coulombic efficiency of nearly 100% under both static and flow conditions.

This study introduces three new triphasic configurations based on all nonaqueous electrolyte systems, utilizing various electrolyte solvents and salts. These configurations exhibit versatility beyond specific redox-active cathode materials. The combinations of electrolyte solvents and salts offer opportunities to explore a wide range of redox-active cathode and anode materials with varying solubilities, paving the way for high-performance membrane-free redox flow batteries. In addition, it effectively addresses issues in conventional RFBs, such as membrane limitations and high costs. Furthermore, it tackles challenges related to self-discharge, low Coulombic efficiency, and crossover of redox materials during electrolyte flow in biphasic membrane-free batteries, demonstrating its broad applicability and improved performance across diverse battery chemistries.

Design of the Nonaqueous Triphasic System. Designing an all-nonaqueous triphasic system with appropriate catholyte and anolyte materials is a significant challenge because of the complex interplay between the solubility of the active material and crossover. To successfully fabricate a high-performance membrane-free redox flow battery using a nonaqueous triphasic (three-layer) system, two primary requirements must be met. First, the three nonaqueous electrolytes must possess immiscibility, high ionic conductivity, and a wide electrochemical stability window. Second, the redox-active cathode material should exhibit high solubility in the catholyte layer and minimal solubility in the intermediate electrolyte layer or the anolyte during both the charging and discharging processes to prevent battery crossover-induced self-discharge. In this study, three triphasic systems were developed, each based on an all-nonaqueous electrolyte: propylene carbonate/NFTTS/1-Butyl-1-methylpyrrolidinium bis(trifluoromethylsulfonyl)imide, benzotrifluoride/1-ethyl-3-methylimidazolium tetrafluoroborate/NFTTS, and TEGDME/NFTTS/FEC (see the Supporting Information for details). However, only TEGDME/NFTTS/FEC was studied for battery analysis due to its relatively lower cost compared with the remaining two systems. Three nonaqueous electrolytes, TEGDME, NFTTS, and FEC, were selected based on their desirable properties, including mutual immiscibility, high ionic conductivity, and key compatibility with Li metal anodes in lithium-ion batteries.[30,35,36] The triphasic systems Design-I and -II were fabricated using the selected electrolytes (TEGDME, NFTTS, and FEC with lithium bis(trifluoromethanesulfonyl)imide (LiTFSI)), as shown in Figure 1A. Before fabricating the triphasic systems, individual electrolyte solutions were prepared for TEGDME, NFTTS, and FEC containing LiTFSI with specific quantities (Figures S1 and S2). The as-prepared electrolyte solutions exhibited

https://doi.org/10.1021/acsenergylett.3c02594
ACS Energy Lett. 2024, 9, 218−225

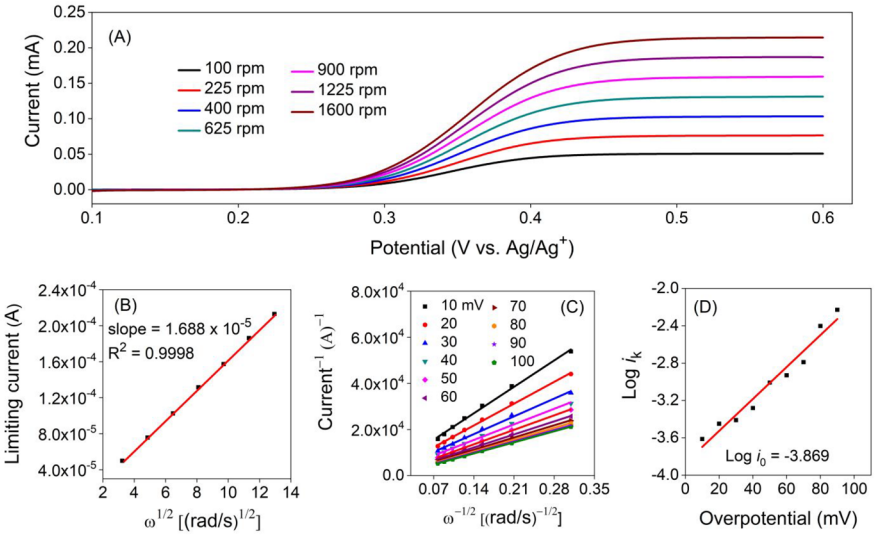

Figure 2. RDE studies of electrolyte solutions containing C18-PTZ (1 mM) in FEC/LiTFSI (0.1 M). (A) LSV curves at a scan rate of 5 mV/s with rotation rates from 100 to 1600 rpm. (B) Fitted linear Lévich plots of the limiting current (i_L) versus the square root of the rotation rates ($\omega^{1/2}$). (C) Linearly fitted Koutecký–Lévich plots of i^{-1} vs $\omega^{-1/2}$. (D) Linearly fitted plots of log i_k as a function of overpotential.

gravimetric densities in the order of FEC/LiTFSI > NFTTS/LiTFSI > TEGDME/LiTFSI. Consequently, in the Design-I triphasic system, the electrolyte solutions were arranged as follows: FEC was the bottom layer, NFTTS was the middle layer, and TEGDME was the top layer (Figures 1A and S3A. The FEC, TEGDME, and NFTTS layers functioned as the catholyte, anolyte, and ion-exchange layers, respectively. Moreover, the NFTTS layer served as the separator, preventing direct contact between the FEC and TEGDME layers while facilitating the desired electrochemical processes.

Utilizing the inherent gravimetric density differences between the as-prepared electrolyte solutions, a Design-II triphasic system was developed using a glass vial with two compartments separated by a common divider (Figures 1A and S3B). Both compartments were filled with the FEC electrolyte solution, and the NFTTS electrolyte solution was added on top of each FEC-containing compartment. In this design, one side of the divider used the FEC electrolyte as the catholyte, whereas the other side used the FEC electrolyte as the anolyte. The strategic positioning of the NFTTS electrolyte as an interfacial layer enabled efficient ion transport and suppressed the crossover of redox species, ensuring the appropriate functionality of the triphasic system while preserving the integrity of the electrochemical processes involved. The triphasic systems constructed in this study according to Design-I and Design-II were thoroughly evaluated for their long-term charge/discharge performances.

Selection of the Anode and Cathode Materials. Achieving a high capacity for RFBs requires the selection of redox-active materials with a high potential. In this study, Li metal was selected as the anode because of its low electrochemical potential (−3.04 V vs a standard hydrogen electrode), high energy density, and theoretical capacity (~3,860 mAh/g).[37] Graphite felt (GF) was selected as the cathode owing to its chemical inertness in nonaqueous electrolytes, high electrical conductivity, highly porous structure, and high specific surface area.[38] To increase the Coulombic efficiency and suppress crossover, the solubility of the catholyte compounds in the catholyte solvent should be high and the solubility in the separating and anolyte electrolytes should be minimal. The solubility properties of several redox-active catholyte compounds, including derivatives of phenothiazine,[22] cyclopropenium,[39] 2,2,6,6-tetramethylpiperidinyloxy (TEMPO),[38,40] anthraquinone (AQ),[41] and ferrocene,[42] were evaluated in the three supporting electrolytes of the triphasic system (Table S1). The phenothiazine derivative **C18-PTZ** (Figure 1B) exhibited high solubility in FEC and poor solubility in TEGDME and NFTTS (see the Supporting Information for details about the solubility tests). The solubility of **C18-PTZ** in FEC/LiTFSI (1.2 M) was determined to be 0.5 M. To investigate the confinement of **C18-PTZ** within the FEC layer, a crossover study was conducted using the triphasic system based on Design-I over a 10-day period under static conditions. The system was evaluated for the potential crossover of 0.5 M **C18-PTZ** dissolved in the FEC phase. Notably, no significant crossover was observed throughout the 10-day period, as confirmed by ultraviolet–visible spectroscopy (Figure S4A) and cyclic voltammetry (CV) (Figure S4B). These results demonstrate the effective confinement of **C18-PTZ** within the FEC layer. Based on these favorable results, **C18-PTZ** was selected as the cathode material for subsequent investigations.

Electrochemical Characterization. CV was used to determine the redox potentials and evaluate the electrochemical stability of **C18-PTZ** in the FEC electrolyte. A well-defined redox couple (0.35 V vs Ag/Ag^+) was observed in FEC/LiTFSI (0.1 M). The almost identical voltammograms obtained after 500 cycles demonstrated the high electrochemical stability of **C18-PTZ** in the FEC/LiTFSI electrolyte (Figure 1C). The peak potential separation of **C18-PTZ** at a scan rate of 50 mV/s was 68 mV, which is indicative of a one-electron redox process as per the Nernst equation.[43] Moreover, the ratios of the cathodic peak current (i_{pc}) and anodic peak current (i_{pa}) at scan rates ranging from 50 to 250 mV/s were approximately 1 (Figure 1D,E), indicating high stability under different scan rates. Furthermore, the anodic and cathodic peak currents had a linear relationship with the square root of the scan rate ($\nu^{1/2}$, Figure S5), indicating that the redox process is diffusion-controlled.[43]

https://doi.org/10.1021/acsenergylett.3c02594
ACS Energy Lett. 2024, 9, 218−225

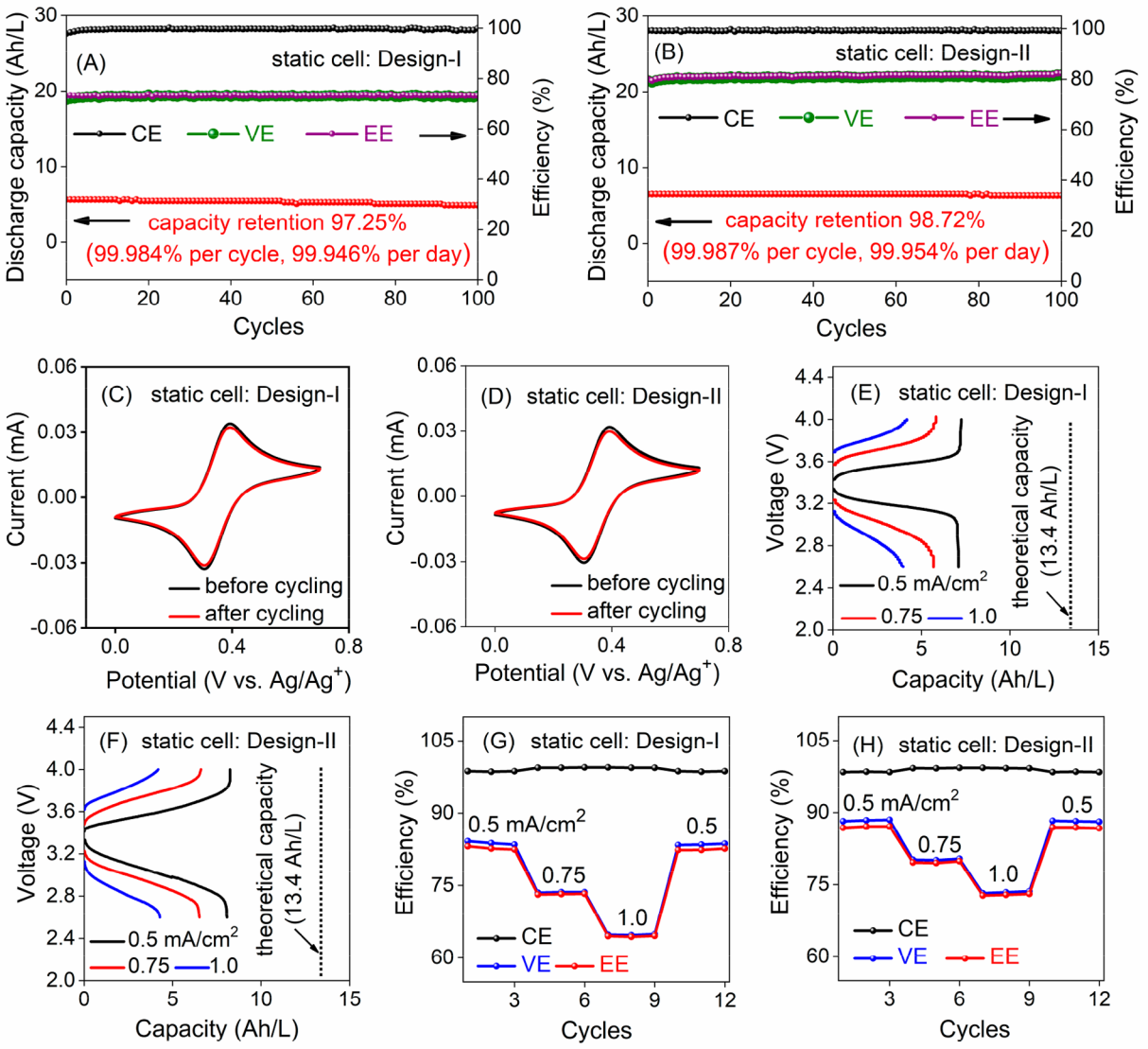

Figure 3. Charge/discharge performances of Li|C18-PTZ (0.5 M) triphasic battery cells under static conditions. Capacity retention, Coulombic efficiency (CE), voltage efficiency (VE), and energy efficiency (EE) values of Li|C18-PTZ (0.5 M) static cells based on (A) Design-I and (B) Design-II. Cyclic voltammograms of the pre- and postcycled catholytes of (C) Design-I and (D) Design-II. Charge/discharge profiles at different operating current densities based on (E) Design-I and (F) Design-II. Coulombic efficiency (CE), voltage efficiency (VE), and energy efficiency (EE) at different current densities for (G) Design-I and (H) Design-II.

The diffusion coefficient D derived from the slopes of the linearly fitted Lévich plots was 6.23×10^{-6} cm^2/s (Figure 2B). The electrochemical kinetic rate constants of the charge-transfer reactions of **C18-PTZ** were obtained using the Kouteck-Lévich equation (eq S2).[43] The linear correlations between i^{-1} and $\omega^{-1/2}$ for **C18-PTZ** at different overpotentials (η = 10, 20, 30, 40, 50, 60, 70, 80, 90, and 100 mV) were used to estimate the i_k values (Figure 2C), which were obtained from the reciprocal of the Y-axis intercepts and plotted against the overpotential, as shown in Figure 2D. The kinetic rate constants (k_0) of **C18-PTZ** were calculated to be 3.51×10^{-3} cm s^{-1} using eq S2. The diffusion coefficients and rate constants of **C18-PTZ** are comparable to those of redox-active organic materials used in aqueous flow batteries.[44−46]

Charge/Discharge Performance. The charge/discharge performances of the nonaqueous triphasic systems (Design-I and -II) using **C18-PTZ** (0.5 M) in FEC (Design-I and -II) as the catholyte and Li metal in TEGDME (Design-I) and FEC (Design-II) as the anolyte were studied under both static and flow conditions. Schematics of the triphasic cell systems are shown in Figures 1A and S6.

Under Static Conditions. Two triphasic cells based on Design-I and -II were assembled by pairing Li metal as the anode and **C18-PTZ** (0.5 M) as the cathode. To evaluate the battery cycling performances of the cells, they were subjected to charging and discharging within the voltage range of 4.0−2.6 V, as the cutoff limits. All charge/discharge experiments were performed in a glovebox filled with an inert Ar atmosphere under normal conditions (27 °C). To evaluate the long-term cycling performances of the cells, they were operated for 100 charge/discharge cycles at a current density of 0.75 mA/cm^2. For the Design-I and -II cells, the operation durations were 28 and 33 days, respectively. Both Li|**C18-PTZ** (0.5 M) triphasic cells exhibited good cycling performances. The capacity retentions of Design-I and -II were 97.25% (99.98% per cycle, 99.94% per day, Figure 3A) and 98.72%

https://doi.org/10.1021/acsenergylett.3c02594
ACS Energy Lett. 2024, 9, 218−225

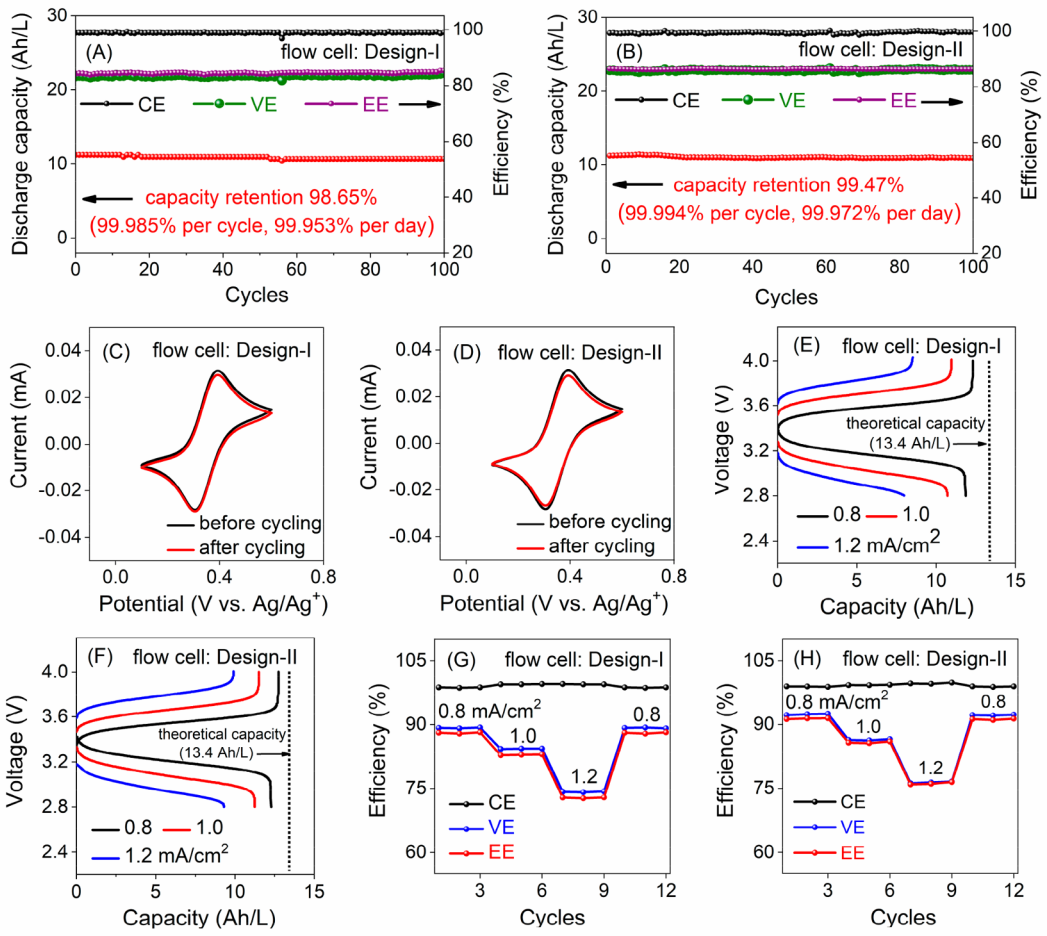

Figure 4. Charge/discharge performances of the Li|C18-PTZ (0.5 M) triphasic battery cells based on Design-I and Design-II under flow conditions. Capacity retention, Coulombic efficiency (CE), voltage efficiency (VE), and energy efficiency (EE) values of the Li|C18-PTZ (0.5 M) flow cells based on (A) Design-I and (B) Design-II. Cyclic voltammograms of the pre- and postcycled catholytes of the Li|C18-PTZ (0.5 M) flow cells based on (C) Design-I and (D) Design-II. Charge/discharge profiles of the Li|C18-PTZ (0.5 M) flow cells based on (E) Design-I and (F) Design-II at different operating current densities. CE, VE, and EE values of the Li|C18-PTZ (0.5 M) flow cells were based on (G) Design-I and (H) Design-II at different operating current densities.

(99.98% per cycle, 99.95% per day, Figure 3B), respectively. The theoretical capacity utilization of the battery cells based on Design-I and -II were measured to be 52.2% and 58.6%, respectively. These results demonstrate that the combination of redox materials (Li and **C18-PTZ**), supporting electrolyte solvents (FEC and TEGDME), and electrolyte salt (LiTFSI) is not only compatible but also stable under real battery operating conditions. Additionally, both static batteries demonstrated high Coulombic efficiencies (approximately 100% for both cells) and energy efficiencies (74% for Design-I and 82% for Design-II), exceeding those of reported membrane-free batteries (80−96%).[22,24,27,28,30] The CV results of the pre- and postcycling electrolytes for both triphasic static cells showed negligible changes in peak current densities (Figure 3C,D), suggesting that **C18-PTZ** remained confined within the catholyte during extended cycling. Thus, the battery cycling performance and postcycling analysis confirmed the importance of the intermediate electrolyte layer (NFTTS) as an ion-exchange separator in the triphasic static system.

To investigate the self-discharge of the static membrane-free batteries, the open-circuit voltage (OCV) of the completely charged cells was monitored for 100 h. The OCV exhibited no significant voltage drop for either battery for more than 100 h. The per-hour voltage loss was 0.45 mV/h for Design-I and 0.53 mV/h for Design-II (Figure S7). Thus, the intermediate layer effectively eliminates self-discharge originating from the migration of the redox species from the catholyte to the anolyte. Moreover, these results demonstrate the high Coulombic efficiency and high capacity retentions of both batteries.

In addition, the effect of various charge/discharge current densities on the performance of the Li|**C18-PTZ** (0.5 M) static cells was investigated. The cells (Design-I and -II) were subjected to cycling at current densities of 0.5, 0.75, and 1.0 mA/cm^2, respectively, and the average Coulombic efficiency, voltage efficiency, and energy efficiency values were determined at each current density over three cycles (Figure 3G,H). The static cells of Design-I and -II exhibited an increase in overpotential with an increasing applied current density. The increase in the overpotential at higher current densities can be attributed to limited mass diffusion.[47,48] Furthermore, both static cells (Figure 3G,H) showed Coulombic efficiencies close to 100%, which is higher than the performances of previously reported membrane-free systems (Table S2). When the applied current density was increased from 0.5 to 1.0 mA/cm^2, the energy efficiency values

https://doi.org/10.1021/acsenergylett.3c02594
ACS Energy Lett. 2024, 9, 218−225

of the batteries decreased from 84% to 64% (Design-I) and 89% to 73% (Design-II). This is caused by the overpotential increase, owing to mass transport losses. Notably, both the batteries regained their original efficiencies when cycled back at 0.5 mA/cm^2, thus confirming their improved charge-rate performances. In addition, the polarization of batteries based on Design-I and -II under static conditions was investigated at different states of charge (SOCs). The peak power densities of the batteries under static conditions were 27 mW/cm^2 (Design-I) (Figure S8A) and 30 mW/cm^2 (Design-II) (Figure S8B) at 100% SOC. Correspondingly, the area-specific resistance (ASR) for both the electrolyte and the entire battery under static conditions (Design-I and Design-II) was also investigated. The ASR of both the electrolyte and the entire battery decreased with increasing SOC. Moreover, the electrolyte contributed more than 60% (Design-I) (Figure S8C) and 53% (Design-II) (Figure S8D) of the resistance compared with that of the entire battery.

To study the cycling stability of the Li anode, we investigated the battery performance (Design-I and Design-II) utilizing a limited amount of Li metal anode (0.9 equiv of the catholyte material) to further assess the efficacy of our developed triphasic electrolyte system. Both batteries underwent 50 charge/discharge cycles (approximately 17 days), with continuous monitoring of their capacity over time. The results indicate that both batteries exhibited capacity retention of 99.17% for Design-I (Figure S9A,B) and 98.12% for Design-II (Figure S9C,D) and Coulombic efficiencies of nearly 100%. CV analysis of pre- and postcycled catholytes and anolytes of batteries based on Design-I (Figure S10A) and Design-II (Figure S10B) suggest negligible crossover of active materials. Moreover, the digital images of pre- and postcycled Li metal anodes of batteries based on Design-I and Design-II (Figure S11) show no signs of dendrite formation. Therefore, the notable capacity retention observed in both batteries demonstrates the good state of health of the Li metal anode and highlights the better efficacy of the developed triphasic electrolyte system.

Under Flow Conditions. While the static triphasic membrane-free batteries demonstrated a notable charge/discharge performance with a Coulombic efficiency of nearly 100% and improved capacity retention, the limited mass-transfer conditions resulted in low capacity utilization. In addition, the independent scaling of energy and power is challenging under static conditions. To evaluate the efficacy of the triphasic system under flow conditions and enable the independent scaling of power and energy, membrane-free triphasic flow cells based on Design-I and -II were evaluated for long-term charge−discharge cycling using a flowing catholyte. The flow conditions were optimized by evaluating the charge/discharge performance of Li‖**C18-PTZ** (0.5 M) flow cells with Design-I (Figure S12A) and Design-II (Figure S12B) at various catholyte flow rates (0.5 to 2.0 mL/min) at a current density of 1 mA/cm^2. Consequently, an optimal flow rate of 1.0 mL/min was selected to perform long-duration cycling. At this flow rate, the flow cells of Design-I and -II showed improved capacity retentions of 98.65% (99.985% per cycle, 99.953% per day) and 99.47% (99.994% per cycle, 99.972% per day), respectively (Figure 4A,B). Design-I (Figure 4A) exhibited a Coulombic efficiency of ∼100%, voltage efficiency of ∼84%, and energy efficiency of ∼83%, whereas Design-II exhibited a Coulombic efficiency of ∼100%, voltage efficiency of ∼88%, and energy efficiency of ∼87% (Figure 4B). No obvious change in the CV current densities of the postcycled batteries was observed, confirming the high stability of the redox-active materials, with no crossover of the active material to the interfacial layer (Figure 4C,D). Both designs exhibited improved performance in terms of efficiency and retention compared with those reported previously (Table S2).

The OCV of the completely charged cells was observed for 100 h to evaluate the effect of electrolyte flow on the self-discharge of the cells (Figure S13A,B). Over the investigated period, minimal decay in the OCV values (0.57 mV/h for Design-I and 0.49 mV/h for Design-II) was observed, which confirmed the absence of self-discharge in the cells. Thus, replacing the biphasic interface with an electrolyte layer can eliminate the interfacial self-discharge and crossover of active materials under convective mass transport by using electrolyte-flowing conditions. The charge rate performances of the Li‖**C18-PTZ** (0.5 M) flow cells based on Design-I and -II were evaluated at current densities of 0.8, 1.0, and 1.2 mA/cm^2, and the corresponding cycling profiles, as well as the Coulombic efficiency, voltage efficiency, and energy efficiency values were measured for an average of three cycles. Similar to the static cells, the flow cells exhibited an increase in overpotential with increasing applied current density (Figure 4E,F). This increase in overpotential is attributed to the induced transport losses that occur at higher current densities.[16,47] The Coulombic efficiency of the cells remained at 100% for all current densities; however, the voltage efficiency and energy efficiency values decayed with an increasing current density. The increase in the overpotential and the corresponding reduction in voltage efficiency at higher current densities may be attributed to mass transport limitations (Figure 4G,H). Both cells regained their original performance when cycled back at 0.8 mA/cm^2. Furthermore, the triphasic cells under flow conditions exhibited improved capacity utilization compared to the static cells (80% for Design-I and 84% for Design-II under flow conditions at 1 mA/cm^2 compared to 42% for Design-I and 48% for Design-II under static conditions at 0.75 mA/cm^2), indicating that the flow of electrolytes significantly reduced the mass transport limitations of the static battery. As a result of the enhanced mass transport, the triphasic batteries exhibited higher peak power densities under flow conditions compared to those under static conditions. Specifically, Design-I achieved a peak power density of 39 mW/cm^2 (Figure S14A), while Design-II reached an even higher peak power density of 46 mW/cm^2 (Figure S14B). The ASR results for both the electrolyte and the entire battery under flow conditions indicated that the electrolyte resistance accounted for over 58% (Design-I) (Figure S14C) and 47% (Design-II) (Figure S14D) of the entire battery. Thus, the ASR of the electrolyte and the entire battery is significantly reduced under flow conditions, allowing for higher current densities without compromising the performance. The relatively low power densities compared to those of conventional aqueous membrane-based redox flow batteries can be attributed to the reduced ionic conductivity of nonaqueous solvents and increased mass transfer resistance from the triphasic interface.

In summary, to overcome the challenges associated with the biphasic electrolyte approach, a triphasic liquid−liquid system with two new strategic designs (Design-I and -II) was proposed. In contrast to biphasic systems, the newly developed triphasic system features an additional electrolyte layer to separate the anolyte and catholyte, eliminating self-discharge and providing high Coulombic efficiency and capacity

https://doi.org/10.1021/acsenergylett.3c02594
ACS Energy Lett. 2024, 9, 218−225

retention. The intermediate layer enabled an improved cycling performance and the flow of the electrolyte to achieve decoupled energy and power. The triphasic batteries based on the two novel designs were assembled using Li metal as the anode and a phenothiazine derivative **C18-PTZ** (0.5 M) as the cathode. The cycling performances of the triphasic membrane-free batteries based on Design-I and Design-II were evaluated under static and catholyte flow conditions. Static batteries based on Design-I and -II yielded outstanding cycling performance with high capacity retentions of 97.25% and 98.72%, respectively, and Coulombic efficiencies close to 100%. However, under static conditions, the capacity utilization of the batteries was lower owing to limited mass transport. To enhance capacity utilization and enable the decoupled scaling of energy and power, flow conditions were introduced for both designs of the triphasic system by using an optimized flow rate of 1 mL/min. Flow batteries based on these designs exhibit a significantly higher capacity utilization than static batteries. Moreover, Design-I and -II flow batteries achieved improved capacity retentions of 98.65% and 99.47%, respectively, with Coulombic efficiencies close to 100%. The peak power densities of the Design-I and -II batteries under static conditions were 27 and 30 mW/cm^2, respectively, whereas those under flow conditions increased to 39 and 46 mW/cm^2, respectively. The improved power densities of the flow batteries were attributed to the lowered electrolyte resistance resulting from enhanced mass transport compared with static batteries. Therefore, the outstanding performance of the nonaqueous triphasic system provides a novel strategy for developing membrane-free, nonaqueous batteries with high voltage, high Coulombic efficiency (close to 100%), improved capacity utilization, and high capacity retention.

■ ASSOCIATED CONTENT

Supporting Information

The Supporting Information is available free of charge at https://pubs.acs.org/doi/10.1021/acsenergylett.3c02594.

Methods; UV−vis spectrum; polarization curve; cyclic voltammograms; performance of battery (PDF)

■ AUTHOR INFORMATION

Corresponding Author

Jianbing Jimmy Jiang − *Department of Chemistry, University of Cincinnati, Cincinnati, Ohio 45221, United States*; Email: jianbing.jiang@uc.edu

Authors

Rajeev K. Gautam − *Department of Chemistry, University of Cincinnati, Cincinnati, Ohio 45221, United States*

Xiao Wang − *Department of Chemistry, University of Cincinnati, Cincinnati, Ohio 45221, United States*

Soumalya Sinha − *Department of Chemistry, University of Cincinnati, Cincinnati, Ohio 45221, United States*; orcid.org/0000-0002-6212-1102

Complete contact information is available at: https://pubs.acs.org/10.1021/acsenergylett.3c02594

Notes

The authors declare no competing financial interest.

■ ACKNOWLEDGMENTS

This study was supported by the National Science Foundation (NSF; Grant No. CBET-2112798). NMR experiments were performed using a Bruker AVANCE NEO 400 MHz NMR spectrometer funded by the NSF-MRI (Grant no. CHE-1726092).

■ REFERENCES

(1) Freire, M. G.; Claudio, A. F.; Araujo, J. M.; Coutinho, J. A.; Marrucho, I. M.; Canongia Lopes, J. N.; Rebelo, L. P. Aqueous Biphasic Systems: A Boost Brought About by Using Ionic Liquids. *Chem. Soc. Rev.* **2012**, *41* (14), 4966−4995.

(2) Dunn, B.; Kamath, H.; Tarascon, J. M. Electrical Energy Storage for the Grid: A Battery of Choices. *Science* **2011**, *334* (6058), 928−935.

(3) Yang, Z.; Zhang, J.; Kintner-Meyer, M. C.; Lu, X.; Choi, D.; Lemmon, J. P.; Liu, J. Electrochemical Energy Storage for Green Grid. *Chem. Rev.* **2011**, *111* (5), 3577−3613.

(4) Lin, K.; Chen, Q.; Gerhardt, M. R.; Tong, L.; Kim, S. B.; Eisenach, L.; Valle, A. W.; Hardee, D.; Gordon, R. G.; Aziz, M. J.; Marshak, M. P. Alkaline Quinone Flow Battery. *Science* **2015**, *349* (6255), 1529−1532.

(5) Soloveichik, G. L. Flow Batteries: Current Status and Trends. *Chem. Rev.* **2015**, *115* (20), 11533−11558.

(6) Wei, X.; Pan, W.; Duan, W.; Hollas, A.; Yang, Z.; Li, B.; Nie, Z.; Liu, J.; Reed, D.; Wang, W.; Sprenkle, V. Materials and Systems for Organic Redox Flow Batteries: Status and Challenges. *ACS Energy Lett.* **2017**, *2* (9), 2187−2204.

(7) Park, M.; Ryu, J.; Wang, W.; Cho, J. Material Design and Engineering of Next-Generation Flow-Battery Technologies. *Nat. Rev. Mater.* **2017**, *2* (1), 1−18.

(8) Wang, W.; Luo, Q.; Li, B.; Wei, X.; Li, L.; Yang, Z. Recent Progress in Redox Flow Battery Research and Development. *Adv. Funct. Mater.* **2013**, *23* (8), 970−986.

(9) Wei, X.; Duan, W.; Huang, J.; Zhang, L.; Li, B.; Reed, D.; Xu, W.; Sprenkle, V.; Wang, W. A High-Current, Stable Nonaqueous Organic Redox Flow Battery. *ACS Energy Lett.* **2016**, *1* (4), 705−711.

(10) Huang, J.; Cheng, L.; Assary, R. S.; Wang, P.; Xue, Z.; Burrell, A. K.; Curtiss, L. A.; Zhang, L. Liquid Catholyte Molecules for Nonaqueous Redox Flow Batteries. *Adv. Energy Mater.* **2015**, *5* (6), 1401782.

(11) Kwabi, D. G.; Ji, Y.; Aziz, M. J. Electrolyte Lifetime in Aqueous Organic Redox Flow Batteries: A Critical Review. *Chem. Rev.* **2020**, *120* (14), 6467−6489.

(12) Ye, C.; Wang, A.; Breakwell, C.; Tan, R.; Grazia Bezzu, C.; Hunter-Sellars, E.; Williams, D. R.; Brandon, N. P.; Klusener, P. A. A.; Kucernak, A. R.; Jelfs, K. E.; McKeown, N. B.; Song, Q. Development of Efficient Aqueous Organic Redox Flow Batteries Using Ion-Sieving Sulfonated Polymer Membranes. *Nat. Commun.* **2022**, *13* (1), 3184.

(13) Gong, K.; Fang, Q.; Gu, S.; Li, S. F. Y.; Yan, Y. Nonaqueous Redox-Flow Batteries: Organic Solvents, Supporting Electrolytes, and Redox Pairs. *Energy Environ. Sci.* **2015**, *8* (12), 3515−3530.

(14) Sevov, C. S.; Brooner, R. E.; Chenard, E.; Assary, R. S.; Moore, J. S.; Rodriguez-Lopez, J.; Sanford, M. S. Evolutionary Design of Low Molecular Weight Organic Anolyte Materials for Applications in Nonaqueous Redox Flow Batteries. *J. Am. Chem. Soc.* **2015**, *137* (45), 14465−14472.

(15) Baran, M. J.; Braten, M. N.; Montoto, E. C.; Gossage, Z. T.; Ma, L.; Chénard, E.; Moore, J. S.; Rodríguez-López, J.; Helms, B. A. Designing Redox-Active Oligomers for Crossover-Free, Nonaqueous Redox-Flow Batteries with High Volumetric Energy Density. *Chem. Mater.* **2018**, *30* (11), 3861−3866.

(16) Jia, C.; Pan, F.; Zhu, Y. G.; Huang, Q.; Lu, L.; Wang, Q. High-Energy Density Nonaqueous All Redox Flow Lithium Battery Enabled with a Polymeric Membrane. *Sci. Adv.* **2015**, *1* (10), No. e1500886.

(17) Nagarjuna, G.; Hui, J.; Cheng, K. J.; Lichtenstein, T.; Shen, M.; Moore, J. S.; Rodríguez-López, J. Impact of Redox-Active Polymer Molecular Weight on the Electrochemical Properties and Transport

across Porous Separators in Nonaqueous Solvents. *J. Am. Chem. Soc.* **2014**, *136* (46), 16309−16316.
(18) Yuan, J.; Pan, Z.-Z.; Jin, Y.; Qiu, Q.; Zhang, C.; Zhao, Y.; Li, Y. Membranes in Non-Aqueous Redox Flow Battery: A Review. *J. Power Sources* **2021**, *500*, 229983.
(19) Montoto, E. C.; Nagarjuna, G.; Moore, J. S.; Rodríguez-López, J. Redox Active Polymers for Non-Aqueous Redox Flow Batteries: Validation of the Size-Exclusion Approach. *J. Electrochem. Soc.* **2017**, *164* (7), A1688−A1694.
(20) Li, X.; Qin, Z.; Deng, Y.; Wu, Z.; Hu, W. Development and Challenges of Biphasic Membrane-Less Redox Batteries. *Adv. Sci.* **2022**, *9* (17), No. e2105468.
(21) Liu, T.; Wei, X.; Nie, Z.; Sprenkle, V.; Wang, W. A Total Organic Aqueous Redox Flow Battery Employing a Low Cost and Sustainable Methyl Viologen Anolyte and 4-HO-TEMPO Catholyte. *Adv. Energy Mater.* **2016**, *6* (3), 1501449.
(22) Chai, J.; Lashgari, A.; Eisenhart, A. E.; Wang, X.; Beck, T. L.; Jiang, J. Biphasic, Membrane-Free Zn/Phenothiazine Battery: Effects of Hydrophobicity of Redox Materials on Cyclability. *ACS Mater. Lett.* **2021**, *3* (4), 337−343.
(23) Wang, X.; Lashgari, A.; Chai, J.; Jiang, J. A Membrane-Free, Aqueous/Nonaqueous Hybrid Redox Flow Battery. *Energy Storage Mater.* **2022**, *45*, 1100−1108.
(24) Navalpotro, P.; Trujillo, C.; Montes, I.; Neves, C. M. S. S.; Palma, J.; Freire, M. G.; Coutinho, J. A. P.; Marcilla, R. Critical Aspects of Membrane-Free Aqueous Battery Based on Two Immiscible Neutral Electrolytes. *Energy Storage Mater.* **2020**, *26*, 400−407.
(25) Navalpotro, P.; Sierra, N.; Trujillo, C.; Montes, I.; Palma, J.; Marcilla, R. Exploring the Versatility of Membrane-Free Battery Concept Using Different Combinations of Immiscible Redox Electrolytes. *ACS Appl. Mater. Interfaces* **2018**, *10* (48), 41246−41256.
(26) Xu, P.; Xie, C.; Wang, C.; Lai, Q.; Wang, W.; Zhang, H.; Li, X. A Membrane-Free Interfacial Battery with High Energy Density. *Chem. Commun.* **2018**, *54* (82), 11626−11629.
(27) Navalpotro, P.; Palma, J.; Anderson, M.; Marcilla, R. A Membrane-Free Redox Flow Battery with Two Immiscible Redox Electrolytes. *Angew. Chem., Int. Ed.* **2017**, *56* (41), 12460−12465.
(28) Navalpotro, P.; Neves, C.; Palma, J.; Freire, M. G.; Coutinho, J. A. P.; Marcilla, R. Pioneering Use of Ionic Liquid-Based Aqueous Biphasic Systems as Membrane-Free Batteries. *Adv. Sci.* **2018**, *5* (10), 1800576.
(29) Meng, J.; Tang, Q.; Zhou, L.; Zhao, C.; Chen, M.; Shen, Y.; Zhou, J.; Feng, G.; Shen, Y.; Huang, Y. A Stirred Self-Stratified Battery for Large-Scale Energy Storage. *Joule* **2020**, *4* (4), 953−966.
(30) Liu, X.; Song, X.; Guo, Z.; Bian, T.; Zhang, J.; Zhao, Y. Biphasic Electrolyte Inhibiting the Shuttle Effect of Redox Molecules in Lithium-Metal Batteries. *Angew. Chem., Int. Ed.* **2021**, *60* (30), 16360−16365.
(31) Gautam, R. K.; Wang, X.; Lashgari, A.; Sinha, S.; McGrath, J.; Siwakoti, R.; Jiang, J. Development of High-Voltage and High-Energy Membrane-Free Nonaqueous Lithium-Based Organic Redox Flow Batteries. *Nat. Commun.* **2023**, *14* (1), 4753.
(32) Wei, X.; Xu, W.; Huang, J.; Zhang, L.; Walter, E.; Lawrence, C.; Vijayakumar, M.; Henderson, W. A.; Liu, T.; Cosimbescu, L.; Li, B.; Sprenkle, V.; Wang, W. Radical Compatibility with Nonaqueous Electrolytes and Its Impact on an All-Organic Redox Flow Battery. *Angew. Chem., Int. Ed.* **2015**, *54* (30), 8684−8687.
(33) Peljo, P.; Bichon, M.; Girault, H. H. Ion Transfer Battery: Storing Energy by Transferring Ions across Liquid-Liquid Interfaces. *Chem. Commun.* **2016**, *52* (63), 9761−9764.
(34) Chakraborty, A.; Bock, R.; Green, R.; Luker, K.; Menard, G.; Sepunaru, L. Split Biphasic Electrochemical Cells: Toward Membrane-Less Redox Flow Batteries. *ACS Appl. Energy Mater.* **2023**, *6* (2), 605−610.
(35) Etacheri, V.; Haik, O.; Goffer, Y.; Roberts, G. A.; Stefan, I. C.; Fasching, R.; Aurbach, D. Effect of Fluoroethylene Carbonate (FEC) on the Performance and Surface Chemistry of Si-Nanowire Li-Ion Battery Anodes. *Langmuir* **2012**, *28* (1), 965−976.
(36) Di Lecce, D.; Carbone, L.; Gancitano, V.; Hassoun, J. Rechargeable Lithium Battery Using Non-Flammable Electrolyte Based on Tetraethylene Glycol Dimethyl Ether and Olivine Cathodes. *J. Power Sources* **2016**, *334*, 146−153.
(37) He, X.; Liu, X.; Han, Q.; Zhang, P.; Song, X.; Zhao, Y. A Liquid/Liquid Electrolyte Interface That Inhibits Corrosion and Dendrite Growth of Lithium in Lithium-Metal Batteries. *Angew. Chem., Int. Ed.* **2020**, *59* (16), 6397−6405.
(38) Wei, X.; Xu, W.; Vijayakumar, M.; Cosimbescu, L.; Liu, T.; Sprenkle, V.; Wang, W. TEMPO-Based Catholyte for High-Energy Density Nonaqueous Redox Flow Batteries. *Adv. Mater.* **2014**, *26* (45), 7649−7653.
(39) Yan, Y.; Vogt, D. B.; Vaid, T. P.; Sigman, M. S.; Sanford, M. S. Development of High Energy Density Diaminocyclopropenium-Phenothiazine Hybrid Catholytes for Non-Aqueous Redox Flow Batteries. *Angew. Chem. Int. Ed.* **2021**, *60* (52), 27039−27045.
(40) Zhao, Y.; Zhang, J.; Agarwal, G.; Yu, Z.; Corman, R. E.; Wang, Y.; Robertson, L. A.; Shi, Z.; Doan, H. A.; Ewoldt, R. H.; Shkrob, I. A.; Assary, R. S.; Cheng, L.; Srinivasan, V.; Babinec, S. J.; Zhang, L. TEMPO Allegro: Liquid Catholyte Redoxmers for Nonaqueous Redox Flow Batteries. *J. Mater. Chem. A* **2021**, *9* (31), 16769−16775.
(41) Wang, W.; Xu, W.; Cosimbescu, L.; Choi, D.; Li, L.; Yang, Z. Anthraquinone with Tailored Structure for a Nonaqueous Metal-Organic Redox Flow Battery. *Chem. Commun.* **2012**, *48* (53), 6669−6671.
(42) Hwang, B.; Park, M. S.; Kim, K. Ferrocene and Cobaltocene Derivatives for Non-Aqueous Redox Flow Batteries. *ChemSusChem* **2015**, *8* (2), 310−314.
(43) Bard, A. J.; Faulkner, L. R.; White, H. S. *Electrochemical Methods: Fundamentals and Applications*; John Wiley & Sons, 2022.
(44) Gao, J.; Amini, K.; George, T. Y.; Jing, Y.; Tsukamoto, T.; Xi, D.; Gordon, R. G.; Aziz, M. J. A High Potential, Low Capacity Fade Rate Iron Complex Posolyte for Aqueous Organic Flow Batteries. *Adv. Energy Mater.* **2022**, *12* (44), 2202444.
(45) Yu, X.; Yu, W. A.; Manthiram, A. High-Energy, Single-Ion-Mediated Nonaqueous Zinc-TEMPO Redox Flow Battery. *ACS Appl. Mater. Interfaces* **2020**, *12* (43), 48654−48661.
(46) Hu, B.; DeBruler, C.; Rhodes, Z.; Liu, T. L. Long-Cycling Aqueous Organic Redox Flow Battery (AORFB) toward Sustainable and Safe Energy Storage. *J. Am. Chem. Soc.* **2017**, *139* (3), 1207−1214.
(47) Li, B.; Gu, M.; Nie, Z.; Wei, X.; Wang, C.; Sprenkle, V.; Wang, W. Nanorod Niobium Oxide as Powerful Catalysts for an All-Vanadium Redox Flow Battery. *Nano Lett.* **2014**, *14* (1), 158−165.
(48) Wang, H.; Sayed, S. Y.; Luber, E. J.; Olsen, B. C.; Shirurkar, S. M.; Venkatakrishnan, S.; Tefashe, U. M.; Farquhar, A. K.; Smotkin, E. S.; McCreery, R. L.; Buriak, J. M. Redox Flow Batteries: How to Determine Electrochemical Kinetic Parameters. *ACS Nano* **2020**, *14* (3), 2575−2584.

https://doi.org/10.1021/acsenergylett.3c02594
ACS Energy Lett. 2024, 9, 218−225